PHYSICAL REVIEW E **88**, 032136 (2013)

Transport and collision dynamics in periodic asymmetric obstacle arrays: Rational design of microfluidic rare-cell immunocapture devices

Jason P. Gleghorn,[*] James P. Smith, and Brian J. Kirby[†]
Sibley School of Mechanical & Aerospace Engineering, Cornell University, Ithaca, New York, USA

(Received 21 May 2013; revised manuscript received 30 August 2013; published 26 September 2013)

Microfluidic obstacle arrays have been used in numerous applications, and their ability to sort particles or capture rare cells from complex samples has broad and impactful applications in biology and medicine. We have investigated the transport and collision dynamics of particles in periodic obstacle arrays to guide the design of convective, rather than diffusive, transport-based immunocapture microdevices. Ballistic and full computational fluid dynamics simulations are used to understand the collision modes that evolve in cylindrical obstacle arrays with various geometries. We identify previously unrecognized collision mode structures and differential size-based collision frequencies that emerge from these arrays. Previous descriptions of transverse displacements that assume unidirectional flow in these obstacle arrays cannot capture mode transitions properly as these descriptions fail to capture the dependence of the mode transitions on column spacing and the attendant change in the flow field. Using these analytical and computational simulations, we elucidate design parameters that induce high collision rates for all particles larger than a threshold size or selectively increase collision frequencies for a narrow range of particle sizes within a polydisperse population. Furthermore, we investigate how the particle Péclet number affects collision dynamics and mode transitions and demonstrate that experimental observations from various obstacle array geometries are well described by our computational model.

DOI: 10.1103/PhysRevE.88.032136 PACS number(s): 05.60.Cd, 47.57.−s, 66.10.C−, 47.63.−b

I. INTRODUCTION

Isolation of rare cells from a heterogenous population has many applications in medical therapies and biomedical research. The quantity of rare cells, for example circulating tumor cells, can guide clinical decision making [1,2]. Additionally, analysis of the molecular and biochemical activity as well as the genetic make-up of rare cells enable mechanistic studies of cell behavior and pathogenesis [3–5]. However, such investigations are limited by the number of cells available and the purity of the cell population. It is difficult to improve both the capture efficiency and purity of rare cell capture systems that use immunospecific surfaces to capture cells but that invariably experience nonspecific adhesion [6]. Thus development of optimized rare cell capture devices involves optimization of the receiver-operator characteristic of the capture physics, simultaneously maximizing target cell capture while minimizing capture of nontarget cells. The ideal system induces target cells to contact the immunocoated surface for as long and as often as possible to increase capture efficiency. However, uniformly increasing cell-wall collisions does not directly improve capture sample purity, as it also exposes nontarget cells to the immunocoated surfaces and increases nonspecific adhesion.

In recent years, microfluidic obstacle arrays have been increasingly used for particle sorting and capture applications. Deterministic ratchets have enabled size-based sorting of microspheres [7,8], viruses [7], and mammalian cells [9–11], and recently, antibody-coated obstacle arrays have been used for rare cell capture from patient blood [12–14]. Microfluidic obstacle arrays have found use because their geometry can be precisely defined and rational design approaches can be used to generate subtle control of device performance. Although much work has been performed to understand how array geometry affects size-based particle displacement [8,15–19], few studies have focused on the effects of these dynamics on surface capture microdevices [12].

Our work has been particularly focused on the ability of obstacle arrays to generate size-dependent particle – wall collision rates that lead to pure and efficient circulating tumor cell capture in complicated samples [3,12]. We refer to the resulting optimization of the receiver–operator characteristic performance of these types of microdevices as geometrically enhanced differential immunocapture (GEDI). In this work, we use a transport – centered design approach to investigate the convection and collision dynamics of a polydisperse particle population in obstacle arrays with varied geometries. This analysis informs the design of immunocapture devices used to capture rare cells from complex samples.

II. DILUTE SUSPENSION, INFINITESIMAL OBSTACLE LIMIT

Fluid transport and related particle forces are important for transport through obstacle arrays; however, many of the central features can be approximated with a ballistic transport model. We describe a ballistic model here and compare to results from simulations with fluid transport in Sec. III. To provide a simplified framework of particle collision dynamics in obstacle arrays, we have developed two-dimensional (2D) ballistic trajectory models for the advection of rigid, circular, diffusionless particles through arrays of infinitesimal obstacles ($2r = 0$). These arrays (Fig. 1) are arranged with obstacles spaced Γ apart from each other in rows perpendicular to flow. Obstacles in subsequent rows are offset from those of the previous row by Δ, and the rows themselves are spaced by a

---

[*] Current address: Department of Chemical & Biological Engineering, Princeton University.

[†] kirby@cornell.edu

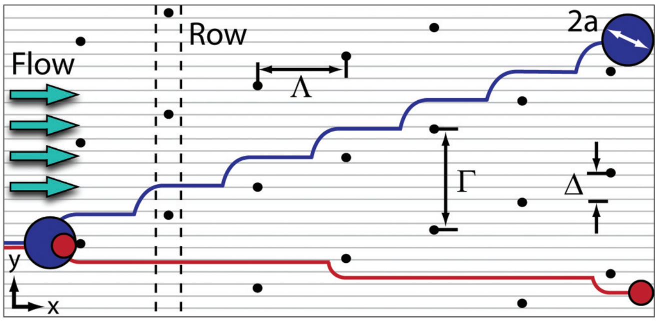

FIG. 1. (Color online) Schematic displaying the pathlines generated by particles of different sizes ($2a$) as they are advected through an array of infinitesimal obstacles (black dots, $2r = 0$) defined by array parameters Γ, Λ, and Δ. Obstacles are arranged in rows perpendicular to flow, and fluid streamlines in this infinitesimal obstacle limit are shown in gray.

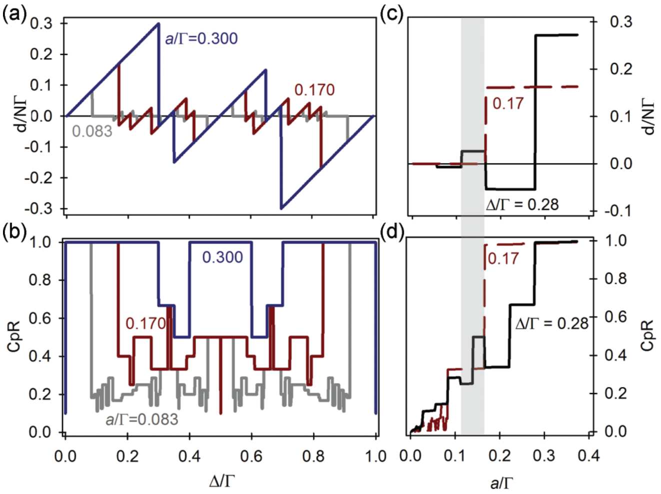

FIG. 2. (Color online) Normalized lateral displacement ($d/N\Gamma$) and the device averaged collisions per row (CpR) from ballistic model simulations (a, b) highlight the complex behavior of particles advected through obstacle arrays. This behavior is size dependent (c, d), and in many instances for any given Δ/Γ different sized particles produce the same lateral displacement with differential collision frequencies (gray shaded region for $\Delta/\Gamma = 0.28$ is one such example). These data are discontinuous; connections between discontinuities are added for clarity.

distance Λ in the direction of flow. Infinitesimal obstacles are convenient because, although they do lead to particle collision when particles have a finite size, in a low-Reynolds-number flow the obstacles perturb the fluid flow only in an infinitesimal region. Thus the flow field and the resulting motion of the particles can be assumed uniform except when particles impact the obstacles. These simplifications result in a uniform flow, and although many physical details are omitted, the behavior of particles in these obstacle arrays captures much of the behavior of real systems. As such, these 2D ballistic trajectory models are an excellent tool for understanding particle collision dynamics and the role of row offsets (Δ) and particle size (a).

Particle motion in these models can be described by noting the particle's transverse position y and the effect that collisions have on that transverse position (Fig. 1). The behavior of a particle as it is transported through an array of infinitesimal obstacles (N rows long) can thus be determined by integrating the effects of a series of impingements on an obstacle, recording the collisions, and recording the deflection when collisions occur. By treating the particles as Lagrangian tracers (particle Stokes number, $\mathrm{St} \to 0$), the collisions with obstacles as inelastic, and the suspension as dilute, the only parameters that control collision performance in these ballistic, uniform flow, infinitesimal obstacle models are a/Γ and Δ/Γ.

A. Transport in infinite arrays

Infinite arrays are defined as obstacle arrays that are infinitely wide and long with a constant lattice geometry. For a specified particle of radius a, its advection through the obstacle array, and therefore both its transverse displacement d and its collision frequency, are dictated by Δ. A particle colliding with an obstacle is transversely displaced to either the left or the right side of the obstacle. For each of these two possibilities, the particle will continue to move through the obstacle array and will impact another obstacle, perhaps after missing a number of rows, to again result in a left or right transverse displacement. The transverse displacement generated from these 2D ballistic trajectory models and, in particular, the particle-size dependence [Fig. 2(a) and 2(c)] is reminiscent of the displacements reported by Frechette and Drazer [18,19]. They used the term "directional locking" to describe the convection of particles though a rotated square array of finite obstacles as calculated with Stokesian dynamics, and, although their array is defined differently from ours, the fundamental dependences of the particle displacement are similar. Although transverse displacement can be used to physically separate particles of different size, this is a fairly insensitive means for identifying rare cells in complex biological samples relative to immunocapture techniques. The performance of immunocapture devices is dependent on interactions between particles and surfaces, rather than particle location in a device; thus the collisions that occur in such a device are important, whereas the transverse displacement is not. Plotting the average collisions per row (CpR) for a range of array geometries (Δ/Γ) [Fig. 2(b)] illustrates that the collision-rate dependence has a more complicated shape and mode structure than the displacement. In fact, the displacement curve is continuous at many Δ/Γ where mode transitions occur and CpR is discontinuous [Fig. 2(c) and 2(d) and Fig. 3]. Most importantly, the collision-rate dependence on Δ and a is neither simple nor continuous. Taken together, the displacement and collision dependences highlight how a specific device design will affect a polydisperse suspension, whereby dramatically different collision frequencies and trajectories can be achieved for particles of a range of sizes.

As these obstacle arrays are periodic, the particle trajectories are also periodic, and we can describe the particle trajectories through the array by use of collision "modes." We denote collision modes using a shorthand notation, in which L, R, and x denote rows in which the particle is deflected to the left, deflected to the right, or has missed the obstacle. This notation describes the periodic collision pattern of coherent particle streams that lead to transverse particle displacement

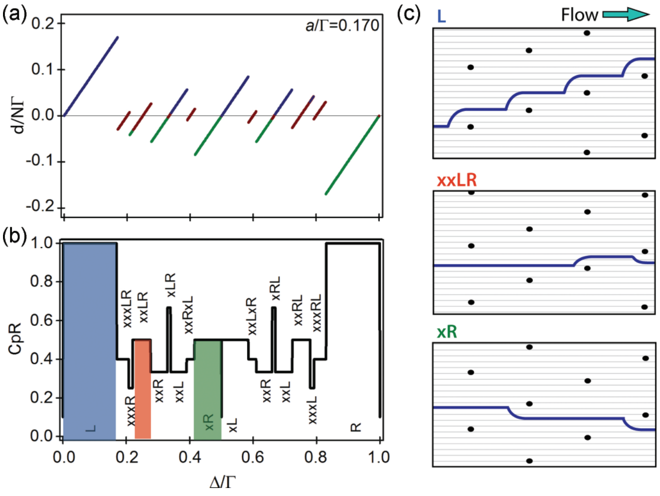

FIG. 3. (Color online) Particles advect through asymmetric obstacle arrays in periodic collision modes. Transverse displacement (a) and collision frequency (b) for $a/\Gamma = 0.170$ are plotted with collision modes indicated in shorthand notation. To aid the reader, color is used on the displacement curve to define pure (nxL: blue, mxR: green) and mixed (nxRmxL: red) collision modes. Whereas CpR directly maps to the collision mode, transverse displacement is continuous at many mode-transition points. Connections in discontinuities in the CpR curve are added for clarity. Particle pathlines for three example modes highlighted in (b) are denoted pictorially in (c).

[Fig. 3(b) and 3(c)]. Thus R denotes that the particle collides with every row, each time being displaced to the right, whereas xxL denotes that a collision occurs every third row and the collision results in a transverse displacement to the left side of the obstacle.

For a given particle radius a and offset Δ, identifying the trajectory of a particle starting on the left or right side of an obstacle is enough to determine its collision mode and collision rate. As the obstacles are in an array, modulo Γ gives the relevant obstacle offset, and thus the criterion regarding whether the particle at y collides with an obstacle that is p rows away from its last collision is given by

$$\mathrm{mod}(|p\Delta - y|\,,\Gamma) < a\,. \tag{1}$$

The sign of $p\Delta - y$ determines the direction the particle is displaced following the collision. After the row location of the next collision is determined as well as the side of the obstacle that is collided with, the mode can be defined as noted in Table I. Here the variables n or m are nonnegative integers denoting the number of rows in which the particle has no collision. Using this formalism, given a, Δ, and examining the trajectory to determine n and m, the mode, the number of coherent streams, and the collision rate (CpR) can be determined as denoted in Table I.

TABLE I. Generalized rules that describe the resulting particle convection mode, number of coherent streams, and collision rate (CpR) for the various collision modes.

After L	After R	Resulting mode	No. of coherent streams	CpR
nxL	mxL	nxL	$n+1$	$\frac{1}{n+1}$
nxR	mxR	mxR	$m+1$	$\frac{1}{m+1}$
nxR	mxL	nxRmxL	$n+m+2$	$\frac{2}{n+m+2}$

B. Transport in finite arrays

The modes as described are defined by what happens *after* a collision; the presence of particles and the effect of collisions limit particles to a fraction of the volume of an array. However, particles initially enter the array randomly distributed and as they progress through the obstacles the particles are displaced into coherent pathlines described by collision modes. This initial ordering phase, prior to obstacle collisions in which particles pass through a fraction of the array, attenuates particle displacements and collision rates. These effects can be ignored in the infinite-array limit; however, the effects are significant in obstacle arrays with finite length. The effects of a finite array can be approximated by calculating the average fraction of the array α during which a particle is in its final steady-state collision mode. The array-averaged collision rate (CpR) for particles is given by the infinite-array result multiplied by α, where $\alpha \longrightarrow 1$ in infinite arrays and $0 < \alpha < 1$ for finite arrays.

As shown in Fig. 4(a), at any position we can calculate the fraction α_0 of particles that have hit an obstacle by that point in the array. As the number of rows increases, a greater fraction of the particles are deflected into their final collision

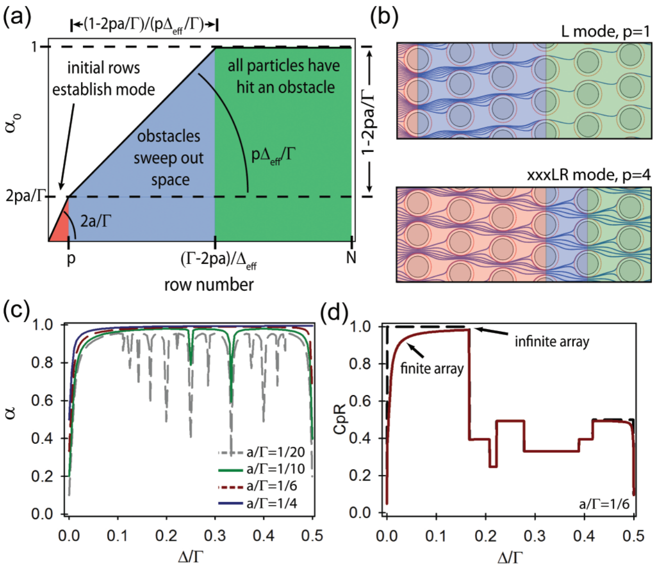

FIG. 4. (Color online) Obstacle arrays with finite length attenuate CpR due to the initial ordering of particles into their collision modes. The attenuation factor α is the area under the curve that represents the fraction of particles that have hit an obstacle α_0 over the number of rows in the array N (a). Two examples illustrate the initial ordering of randomly oriented particles as they enter an obstacle array and form coherent particle streams (b). Examples are drawn with finite obstacles and pathlines result from convection in a Stokes flow to aid in visualization of the physical mechanism occurring in real devices. The finite-array correction factor α plotted for differently sized particles (c). An example CpR curve for a finite array (solid curve) obtained by multiplying CpR for an infinite array (dotted curve) by α (d). α and CpR are plotted over $0 \geqslant \Delta/\Gamma \leqslant 0.5$ because these curves (and $d/N\Gamma$) are symmetric about $\Delta/\Gamma = 0.5$.

mode eventually reaching $\alpha_0 = 1$. For a given array geometry, we use the symbol p to denote the maximum number of rows until a subsequent collision (e.g., R, $p = 1$; xL, $p = 2$; xxRxL, $p = 3$). We call this the mode number. Initially, as an evenly distributed front of particles enters an array and advects through the first p rows, a fraction of the particles $(2ap/\Gamma)$ will collide with the obstacles. Subsequent rows of obstacles then sweep out the remaining space [Fig. 4(b)]; colliding with the remaining particles until all particles have been deflected into their steady-state collision mode. The finite-array correction factor α is the average, along the length of the array, of the fraction of particles that have collided with an obstacle; it is given by $\alpha = \frac{1}{N}\int_1^N \alpha_0\, dx$, where x is the row number.

For an array with N rows (where $N \gg 1$), if $N < \frac{\Gamma - 2ap}{\Delta_{\text{eff}}}$, a fraction of the particles never collides with an obstacle, and α is given by

$$\alpha = \left(1 - \frac{p}{2N}\right)\left(\frac{2ap}{\Gamma} + \frac{N\Delta_{\text{eff}}}{2\Gamma}\right)$$
$$\Delta_{\text{eff}} = p * \min[\bmod(\Delta, \Gamma/p), \quad \bmod(\Gamma/p - \Delta, \Gamma/p)] \tag{2}$$

As the array can be offset up (positive y direction) or down (negative y direction) and Δ is always referenced in the positive y direction, Δ_{eff} is needed to to determine the distance between Δ and the nearest Γ/p.

For an array $N \geqslant \frac{\Gamma - 2ap}{\Delta_{\text{eff}}}$, all of the particles are in their final collision modes at the outlet, and α accounts for both the period during which the obstacle array is sweeping out the volume and the period during which particles are in their modes:

$$\alpha = \left(1 - \frac{p}{2N}\right)\left[\frac{2ap}{\Gamma} + \left(1 - \frac{2ap}{\Gamma}\right)\left(1 - \frac{\Gamma - 2ap}{2N\Delta_{\text{eff}}}\right)\right]. \tag{3}$$

With these analytical results, we can observe the performance of the correction factor α as a function of particle size and offset [Fig. 4(c) and 4(d)]. For large particles, one mode number is observed and the curve has minima only at $\Delta = 0$ and $\Delta = \Gamma$, whereas for smaller particles the curve has more minima and a lower peak value $(1 - \Gamma/4Na)$.

The location of these minima in α occur at a/Γ values that are rational fractions, e.g., 1/2, 1/3, 2/3, and they are important in part because they correspond to offsets that are the most convenient for CAD design when making a design for a microfluidic device. To design a device with many rows of obstacles, the easiest procedure is to have the offset be a rational fraction of $n\Gamma$ and use a cut-and-paste operation to complete the obstacle array. This procedure would effectively produce the worst possible design, corresponding to minima in collision rates and in many cases such offsets also curtail differences in CpR between differently sized particles.

C. Transport in reversing arrays

Whereas a number of investigators have focused on the displacement caused by obstacle arrays on particles and, in particular, the size dependence of this effect [7,8,15,18,19], the use of obstacle arrays for rare cell capture [12–14] motivates geometries that maximize collisions for target particle sizes and reduce collisions for particles of unwanted size. If the goal is to capture particles with a broad spatial input distribution, displacement transverse to the flow is of little use and in fact reduces the effectiveness of the array over time as the particles of interest are often deflected to the edge of the array. Because of this, optimal designs would minimize transverse deflection. This can be achieved by reversing the row offset periodically [Fig. 5(a)]. We define a reversing array such that after every N_r rows, the row is offset by a distance Δ^* and the rows to follow have offsets equal to $-\Delta$. This pattern with repeating regions of posts offset by $\pm\Delta$ continues along the length of the array.

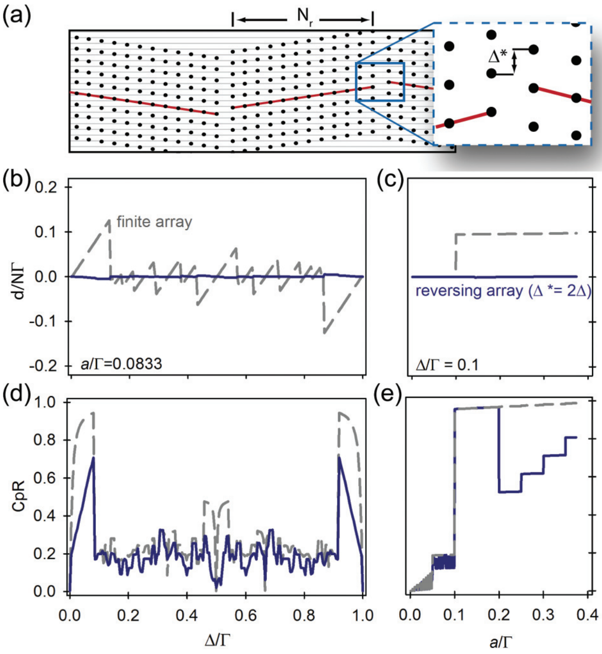

FIG. 5. (Color online) Reversing arrays defined by repeating array segments (of length N_r with $\pm\,\Delta$) that are offset by Δ^*(a) can be used to minimize transverse displacement (b, c) and alter CpR (d, e). Reversing arrays can produce a notch filter such that CpR is increased for a narrow range of particle sizes within a polydisperse population. Dashed lines represent a finite nonreversing array and solid lines are ballistic results from a reversing array with $\Delta^* = 2\Delta$.

For particle convection through infinite, nonreversible obstacle arrays, all particles are assumed to be in their long-time limit in which they are repeatedly colliding with obstacles following their mode pattern. However, in reversing arrays, particles are advected through a series of finite obstacle arrays, and therefore CpR is highly dependent on the position of the coherent particle streams as they exit an obstacle section and enter the subsequent reversed section. As such, the offset at reversal Δ^* provides an additional parameter that affects the CpR vs a/Γ curve and can be used to to create additional size-dependent responses. The effect of reversing the array is nil when Δ^* is chosen to put the particles back into the same mode; this is observed for $\Delta < a < 2/\Delta^*$. If Δ^* is chosen so that particles of interest fall into this range, then reversing the array minimizes the transverse displacement [Fig. 5(b) and 5(c)] and transitions the CpR response of the system from a high-pass filter to a notch filter [Fig. 5(d) and 5(e)]. If chosen otherwise, the CpR is attenuated because particles are affected by the finite-array CpR attenuation every time the array reverses. A reversing array, therefore, has great utility for increasing the collision frequency of a narrow range of particle sizes within a polydisperse population.

III. DILUTE SUSPENSION, FINITE-SIZE, Pe = ∞ OBSTACLE LIMIT

The ballistic model applicable for infinitesimal obstacles provides a framework for interpreting simulated or observed CpR results but does not incorporate obstacle effects on flow and fluid-particle forces. In real devices, the presence of obstacles with finite size perturbs the fluid velocity field and therefore alters particle transport through the array. CFD models were used to solve for the resulting velocity field, and a custom advection algorithm was used to track particle trajectories in finite-sized obstacle arrays with various geometries.

Simulations were performed using a 2D unit-cell approach. An array of five obstacles in the direction normal to flow and 13 perpendicular to flow was used to calculate the flow field in the unit cell around the central obstacle. The 2D assumption is appropriate only if the microdevice height is much larger than the gap between the obstacles ($h \gg \Gamma - 2r$) and the assumption that the inlet flow is uniform is appropriate only if the flow resistance of the inlet and outlet channels is large in comparison to the obstacle array.

The fluid velocity field through the obstacle array was calculated by solving the Navier-Stokes equation over the domain. Velocity boundary conditions were applied at the inlet ($100\ \mu\mathrm{m/s}$) and solid boundaries (no-slip, $u = 0$), whereas the outlet boundary condition was handled by use of a velocity gradient ($\partial u/\partial n = 0$). Although the full Navier-Stokes equations were solved in dimensional form, all simulations satisfied the Stokes approximation ($\mathrm{Re} \ll 1$) and the resulting velocity field is interpreted in nondimensional form ($u^* = u/u_{\mathrm{inlet}}$).

Particle trajectories were calculated using custom Matlab code with the particle position integrated forward in time through the array with a fourth-order Runge-Kutta scheme. A no-penetration condition was prescribed at the obstacle wall with a quadratic potential field penalty function. Additional particle-wall interactions, including lubrication forces, were not addressed directly; instead the aforementioned surface penalty function served as ad hoc accounting of transverse forces for flow parallel to walls with an approaching particle. Particle start positions were uniformly distributed along the first unit cell boundary, and all computational data presented herein result from advection of particles through 100 rows of the nonreversing obstacle array. Particle advection was assumed to be diffusionless (Péclet number, $\mathrm{Pe} \to \infty$), and particles were treated as Lagrangian tracers ($\mathrm{St} \to 0$). Numerical error tolerances and integration time steps were adjusted such that solution convergence was achieved, and numerical diffusion of the particles was observed to be $10^{-24}\ \mathrm{m^2/s}$, a diffusivity much smaller than the diffusion coefficient associated with Brownian motion for these particles ($10^{-14}\ \mathrm{m^2/s}$).

A. Collision modes as a function of obstacle array geometry

In the finite-sized obstacle limit, the array geometry defines the flow field and the resulting particle transport through the array. The five lengths that govern this flow are Γ, a, Δ, Λ, and the obstacle diameter $2r$, which we organize into four nondimensional parameters: the array constant Γ/Λ and the nondimensional particle radius a/Γ, offset Δ/Γ, and obstacle diameter $2r/\Gamma$. We explore the effects of these geometric parameters on CpR by altering variables from a datum state ($a/\Gamma = 1/8$, $\Delta/\Gamma = 1/6$, $2r/\Gamma = 2/3$, and $\Gamma/\Lambda = 1$) in a finite nonreversing array and evaluating over $0 \leqslant \Delta/\Gamma \leqslant 0.5$ because of the symmetry in the CpR curve.

The full CFD simulations produce results that are similar to those from the ballistic analysis [Fig. 6(a)]. The uniform velocity profile in the ballistic simulation is consistent with a geometry where the depth is small relative to Γ and $2r/\Gamma$ (i.e., a Hele-Shaw geometry) and is described by the Laplace equation. The full CFD simulation models a tall device in the regions away from the floor and the ceiling and is best

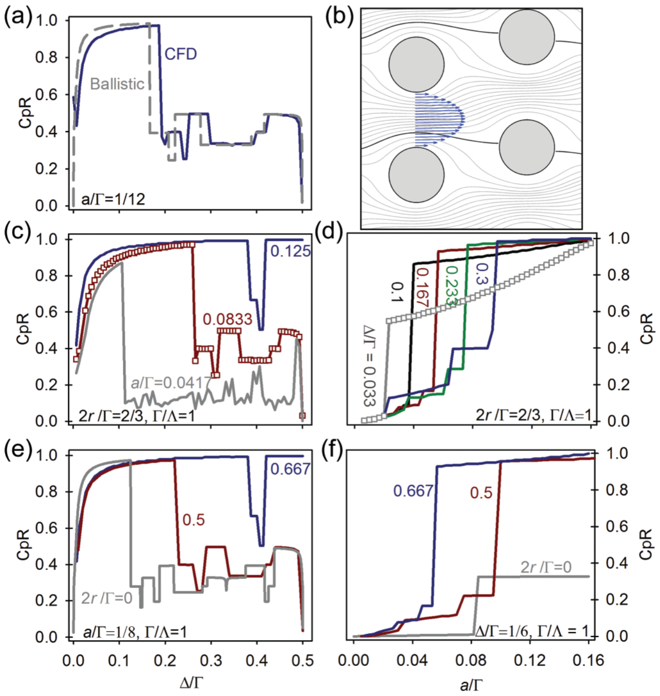

FIG. 6. (Color online) Collision dynamics for particles advected though an array of finite-sized cylindrical obstacles (CFD model) compared with infinitesimal obstacles (ballistic model) (a). The flow field through a finite-sized obstacle array (gray streamlines, stagnation streamline is black) is nonunidirectional and nonuniform with an approximately parabolic velocity distribution in the gap between posts (b). Particles with a center below the stagnation streamline follow the stream tube around the subsequent obstacle whereas larger particles are carried by the bulk flow in a direction that follows the orientation of the array obstacles as defined by Δ/Γ. CpR results for particles advected with CFD models investigating effects of particle size (c), offset (d), and obstacle diameter (e, f). CFD results are drawn as lines for clarity; however, individual data points are shown for $a/\Gamma = 0.0833$ (c) and $\Delta/\Gamma = 0.033$ (d) to indicate the frequency of sampling of the Δ/Γ and a/Γ parameter spaces used to resolve transitions in CpR for all CFD simulations.

described by the 2D Navier – Stokes equations. The addition of the fluid velocity field in the full simulations causes a slight shift in the location of transitions between modes; however, the collision-rate and displacement magnitudes (data not shown) are well predicted by the ballistic model even though it does not capture all effects of the fluid flow on particle trajectories. Although full CFD simulations lead to results that are slightly distorted from the ballistic models described thus far, these ballistic models nonetheless provide an efficient and intuitive description of the mode structure of the system response.

As expected, the velocity field generated by finite obstacles leads to alterations in the collision dynamics [Fig. 6(c)–6(f)]. The effect of fluid mechanics on the ability of the ballistic trajectory model to predict mode thresholds varies depending on the nature of the mode transition. This is attributable to two errors, which largely cancel over much of the parameter space. One error of the ballistic model is the uniform velocity profile, which deviates from the actual (approximately parabolic) flow profile, and a second error is the assumed unidirectionality of the flow. Relative to the the flow between infinitesimal obstacles, flow between finite obstacles is rotated along $\sin^{-1}(\Delta/\Gamma)$ (for most of the gap cross section) whereas a small portion of the flow (near the obstacle edge) is rotated counter to this direction to satisfy the net unidirectionality of the integrated flow [Fig. 6(b)]. As such, larger particles follow pathlines that move in the direction of the bulk flow, whereas smaller particles, with a particle center closer to the obstacle than the stagnation streamline, follow streamlines that pull the particle around to the other side of the subsequent obstacle. This flow profile causes the shift in mode transitions from those observed in the ballistic simulations. The tendency of larger particles to remain in the L mode, for example, is made more extreme by the finite-diameter obstacles as the particle center remains in the array-aligned bulk flow [Fig. 6(c)].

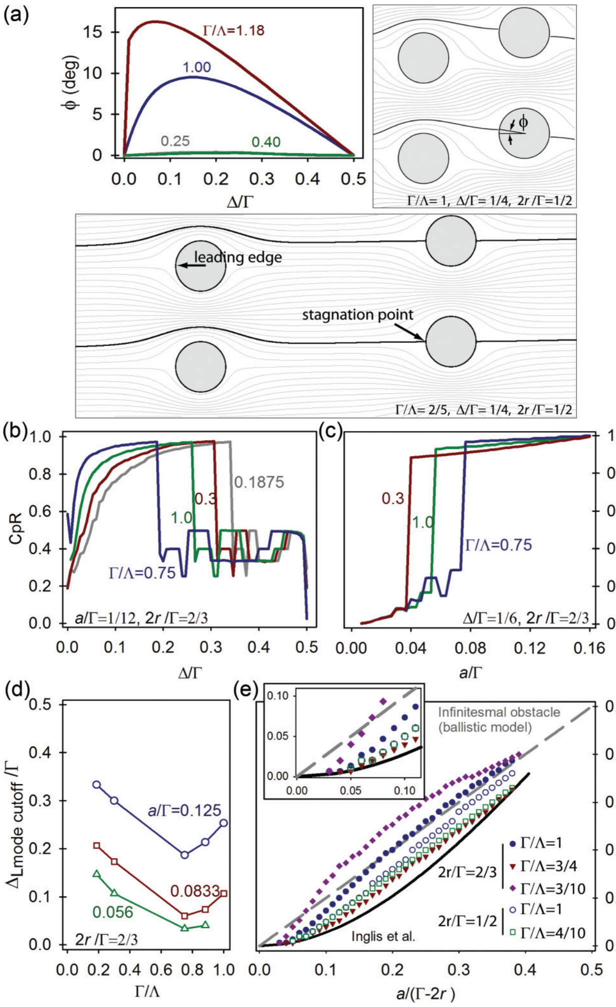

FIG. 7. (Color online) Due to the nonunidirectional nature of the flow, the position of the stagnation streamline in the gap between obstacles and the angle of incidence of the stagnation streamline relative to the leading edge of the obstacle, ϕ varies with the array parameter Γ/Λ (a). This results in altered collision dynamics with Γ/Λ (b, c). As one example of the variabilty in the transitions with Γ/Λ we investigate the Δ/Γ parameter that defines the the transition out of the L collision mode (d). The nonuniformity in the flow field prevents a general parametrization to collapse the data with Γ/Λ (e). Data shown for Γ/Λ values indicated in (e) for $2r/\Gamma = 2/3$ (filled symbols) and $2r/\Gamma = 1/2$ (open symbols).

The directionality of the flow field that arises with finite obstacles has not been included in previous analyses [8,15–17,20,21]. These studies have ignored Λ as a parameter as they typically examine square arrays ($\Gamma = \Lambda$) and therefore do not account for the array parameter Γ/Λ. However, the angle of incidence of the stagnation streamline relative to the leading edge of the obstacle does change with Γ/Λ [Fig. 7(a)]. The nonunidirectional nature of the flow varies the position of the stagnation streamline in the gap between the previous row of obstacles. This leads to significant effects on the collision modes with CpR varying with Γ/Λ at fixed Δ/Γ [Fig. 7(b)]. Furthermore, these changes do not exhibit monotonic dependence on Γ/Λ, as is illustrated by plotting the transition point out of the L mode $\Delta_{\text{Lmode cutoff}}/\Gamma$ as a function of Γ/Λ [Fig. 7(d)]. Inglis and coworkers analyzed deterministic lateral displacement obstacle arrays by presuming a parabolic distribution of velocity between obstacles and relating flow rates and streamline locations to particle diameters with specific attention to the L mode cutoff. This analysis, which assumes that the flow is unidirectional in the direction of flow, leads to the conclusion that the particle trajectory is dependent only on the location of the particle center with respect to the parabolic distribution. The location of the particle center can be parameterized using $\frac{a}{\Gamma-2r}$ or, equivalently, $\frac{a/\Gamma}{1-2r/\Gamma}$. If we examine the L-mode cutoff as a function of the particle center [Fig. 7(e)], we see that Inglis's parametrization captures the contraction and dilation of the streamlines by assuming a parabolic flow, but it does not capture the directionality of the flow, as the curves do not collapse with Γ/Λ. For the L-mode transitions, the streamline expansion associated with the approximately parabolic flow profile cancels the flow tilt to first order near the stagnation streamline. Thus a ballistic model (which ignores both) gives good predictions. Models that incorporate flow nonuniformity but not nonunidirectionality are arguably physically more accurate but, in our simulations, underperform as they do not have this error cancellation. For other mode transitions, the net effect of the flow nonuniformity and nonunidirectionality leads to a more complicated effect. This results because the fluid physics leads to a nonlinear transform to the fluid particle locations, and the mode transitions (which, absent fluid transport in the ballistic limit, are described by linear displacement equations) are more difficult to predict. Phenomenological adjustments can be used to approximate these effects, but we have not been able to determine a general linear transform for this correction.

IV. DILUTE VERSUS DENSE SUSPENSIONS: EFFECT OF DIFFUSIVE TRANSPORT

In a dilute solution, particle – particle interaction is minimized and Brownian diffusion is the main departure from our Lagrangian model. For obstacle arrays used to induce transverse displacements [7,8,17,18], optimal performance occurs with high flow rates that increase the particle Péclet number (Pe) and thereby enable deterministic displacements. However, in immunocapture systems, high flow rates decrease the residence time the particle has with an immunocoated surface and increases the hydrodynamic shear stresses. This, in turn, decreases the overall performance of the system. As such, diffusive transport in lower-Pe flows is important to consider for immunocapture applications.

In a system designed for rare cell capture, the cell size ranges from 5 to 25 μm and as such, even with low flow rates needed for immunocapture applications (mean velocities $\sim$ 100 μm/s), the Pe is relatively high. In these dilute suspensions, Pe exceeds 10^5 for typical rare cell capture microdevices [22]. However, in many applications of immunocapture, the desire to isolate specific cell populations from heterogenous samples necessitate processing of dense cell suspensions. This is particularly true for applications of rare cell capture from blood, in which cell densities are on the order of 10^6 cells/μl (hematocrit, Hct $\sim$ 0.5). In these dense suspension flows, particle – particle interactions cannot be ignored as in the dilute limit. In fact, these particle interactions coupled with the size and heterogeneity in the mechanical properties of the cells lead to interesting phenomena in blood, including the Fahraeus effect and margination [22,23], which affect transport of cells within the flow field. Additionally, dense suspension flows exhibit shear-induced diffusion (SID) [24–28] whereby particle – particle interactions, due to different relative speeds along streamlines, result in displacements from the average trajectories. In monodisperse suspensions, the resulting SID or dispersion is dependent on the particle density and is proportional to the particle size and the shear rate of the suspending fluid ($\sim 2a^2\dot{\gamma}$) [24,29]. In dense suspensions of red blood cells, the diffusivity increases by approximately two orders of magnitude ($D \sim 10^{-12}$ m^2/s) [24,28,30]. SID is a primary source of diffusion for cells in whole blood; however, blood is a complex polydisperse suspension, and a rigorous analysis for polydisperse suspensions of deformable particles is not available. From studies of bidisperse suspensions that investigated SID of a low volume fraction of larger tracer particles in a dense suspension of smaller particles, it was determined that SID of the tracer particles decreased as the ratio of particle sizes ($a_{\text{tracer}}/a_{\text{suspension}}$) increased [31]. As such, we would expect the SID for much larger blood cells, including leukocytes and circulating tumor cells, to be significantly less than the dispersion of red blood cells. Given the low shear rates calculated from our CFD simulations (volume averaged: 5.31 s^{-1}) and the geometries for other typical rare cell capture microdevices found in the literature [22] we estimate that the particle Pe of target cells in whole blood would decrease by an order of magnitude (10^4–10^5) relative to the dilute limit.

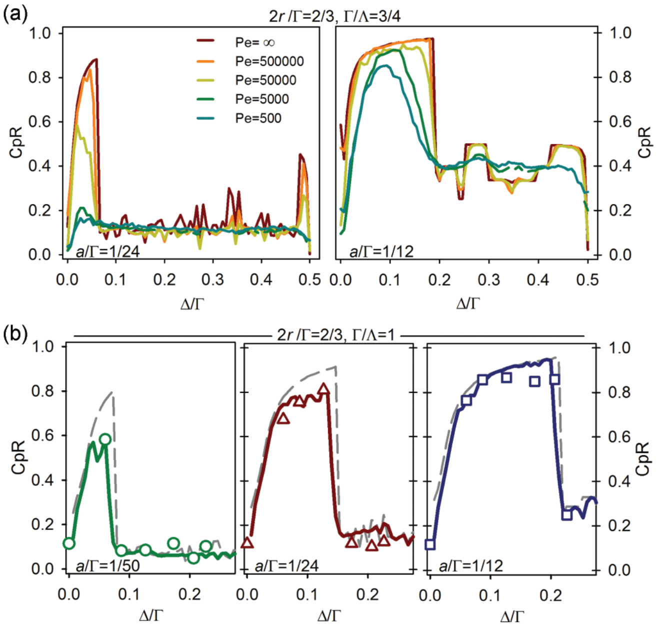

FIG. 8. (Color online) The effects of varying Péclet number, Pe, on the collision frequencies for two different particle sizes (a). Experimentally measured CpR of individual particles tracked through a small portion of an array (symbols) are well described by CFD simulations (b) that account for Brownian motion of the particle (solid line). Gray dashed line represents full CFD simulation data with Pe $= \infty$ for comparison.

For the purposes of the current work, we have asked how alterations in the Péclet number that result from any number or combination of the mechanisms described would alter the CpR response of the system. The effect of diffusion on the transverse displacement has been studied theoretically previously [17,32,33], and thus we focused on the effects to collision frequency. We have altered the Pe of the full CFD simulations by adding Brownian diffusion to the particle transport equations, with a randomly oriented displacement calculated from the diffusivity applied to the particle trajectory at each time step. As such, the effective diffusivity, $D_{\text{eff}} = 0$ corresponds to the dilute suspension, infinite Pe limit where particles are modeled as Lagrangian fluid tracers.

Decreasing the Péclet number causes a smoothing of the CpR curve with less sharp transitions between collision modes [Fig. 8(a)]. As the Péclet number decreases, transport through the device and the resulting collision frequencies become less deterministic. This reduces the size-dependent differences in collision frequency for a given obstacle array geometry. For lower-Pe flows, choosing a larger value for a/Γ is beneficial primarily because of the mode structure of the CpR curve. Smaller a/Γ generates more complex collision patterns with a greater number of higher order modes available to a given particle. As such, transitions between modes are more frequent, and the effect of particle diffusion has greater consequences to the collision frequency. Larger a/Γ has fewer collision modes and thus dispersive perturbations to the particle advection results in minor alterations to the CpR curve.

To determine if these simulations describe experimental observations, experiments were conducted in the dilute-suspension limit and compared to CFD simulation data with a D_{eff} equal to the Brownian-motion-induced diffusivity for a given particle diameter [Fig. 8(b)]. Device fabrication and experimental conditions were the same as those described previously [3,12]. Briefly, cylindrical obstacle arrays were etched into silicon (etch depth ~100 μm, $\Gamma = 150$ μm, $\Gamma/\Lambda = 1$, $2r/\Gamma = 2/3$) and placed into a plexiglass jig that clamps a polydimethylsiloxane (PDMS) cover onto the device to create a sealed microfluidic obstacle array. A single inlet port branches into a ramified network of channels such that the sample is uniformly distributed across the width of the array and a symmetric series of channels at the end of the array similarly channel fluid to a single outlet. Polystyrene microspheres with sizes similar to blood cells (Bangs Laboratories; 10.11 ± 0.703 μm, 15.50 ± 1.52 μm, and 20.92 ± 0.64 μm) were diluted to a 0.42% volume fraction in a density-matched deionized water/glycerol solution (1.062 g/ml) to eliminate gravitational settling. The suspension of microspheres was processed through the device at a flow rate of 1 ml/h. Individual particles were manually tracked as they traversed ten rows of obstacles, their collisions were recorded, and CpR for the population was calculated [CpR = total collisions/(10×number of particles)]. Δ/Γ values for the fabricated devices were chosen to capture the transition between the L mode and higher-order modes for each microsphere size. Experimental data in the dilute limit is well described by our simulations that account for Brownian motion of the particles [Fig. 8(b)], capturing both the CpR magnitude and the transition out of the L mode. Whereas our experimental data is only in the dilute limit owing to challenges in recording collision dynamics within dense suspensions, this analysis framework has been successfully used previously [3,12] to design GEDI devices that capture cells from dense cell suspensions. We have found that designing geometries that have maximized the $\mathrm{CpR}_{\text{target cell } a}/\mathrm{CpR}_{\text{nontarget cell } a}$ ratio have generated significant improvements in capture efficiency (40% increase, 85% efficiency) and purity (37% increase, 68% purity) of rare cells from whole blood [12]. As such, in spite of the decreased Pe that results from dense suspensions advected through these immunocapture microdevices, these design principles enumerated herein are still relevant and effective for immunocapture of cells from dense suspension such as whole blood.

V. CONCLUSION

Fundamentally, microdevice-based immunocapture can be thought of as a superposition of physical challenges (transporting cells to immunocoated surfaces, maximizing residence time at those surfaces, and minimizing hydrodynamic forces) and chemical challenges (ligand-binding kinetics, specificity, and surface stereochemistry). The work described herein focuses on a physical aspect of the problem: designing microdevice geometries that preferentially maximize the transport of target cells to capture surfaces.

The shift in thinking for rare cell immunocapture [14] from immunocoated surfaces and channel walls (effectively two-dimensional thinking) to the use of immunocoated obstacles staggered throughout the flow (taking advantage of the third dimension) has produced a dramatic increase in the performance of immunocapture devices. Often, the argument for the design of these devices is one based upon diffusive transport: increasing the surface area to volume ratio with dense obstacle arrays thereby decreasing the critical diffusion length to antibody-coated surfaces. However, in using this approach an opportunity is lost to leverage fluid mechanics to deterministically aid in immunocapture as is demonstrated in geometrically enhanced differential immunocapture (GEDI) microdevices [3,12]. In this context, we have built upon the work of others [7,8,15,17–19] that have investigated transverse particle displacements to design deterministic lateral displacement (DLD) obstacle arrays.

As high-performance immunocapture devices require slower flow rates and often the processing of dense polydisperse cell suspensions compared to DLD systems, diffusive perturbations from convective pathlines cannot be ignored. Altering the Pe of the flow in CFD simulations attenuates the overall CpR curve; however, in the operating regimes for these devices, size-based differences for larger a/Γ values are robust. Experimental data are well predicted by CFD simulations in the dilute limit, and trends in capture efficiency of target cells from dense suspensions of whole blood reported herein and previously published [3,12] are consistent with predicted CpR.

Whereas previous work has not focused on the particle-obstacle collision dynamics in microfluidic obstacle arrays, we have identified a rich mode structure in the collision frequency response of the system that is nonintuitive but produces deterministic collision patterns. Furthermore, investigating only transverse displacement is not sufficient to understand the collision dynamics, as multiple collision modes produce the same transverse displacement (L, Lx, Lxx, etc.) but different CpR. Our results describe the effects that alterations in obstacle array geometry have on CpR and demonstrate the ability to generate differential collision frequencies based on particle size. Unlike DLD obstacle arrays that focus on a critical particle size, above which all larger particles are laterally displaced, we have demonstrated that the array geometry can similarly induce high collision rates for all particles above a threshold size (nonreversing array) or selectively increase CpR for a narrow range of particle sizes (reversing array) within a polydisperse population. Continued advancements in convective transport-based immunocapture systems, GEDI microdevices, are important as this technology has broad utility for a number of disciplines in cell biology and medicine with applications ranging from isolation and enrichment of stem cell populations to identification of cells with disease-specific surface antigens to the enumeration of cancer cells from clinical blood samples.

ACKNOWLEDGMENTS

This work was supported by the Center on the Microenvironment and Metastasis (CMM) at Cornell, a Physical Sciences Oncology Center (PS-OC) supported by the National Cancer Institute under Award Number U54CA143876.

[1] V. Muller, S. Riethdorf, B. Rack, W. Janni, P. A. Fasching, E. Solomayer, B. Aktas, S. Kasimir-Bauer, K. Pantel, and T. Fehm, Breast Cancer Res **14**, R118 (2012).
[2] D. R. Parkinson *et al.*, J. Transl. Med. **10**, 138 (2012).
[3] B. J. Kirby, M. Jodari, M. S. Loftus, G. Gakhar, E. D. Pratt, C. Chanel-Vos, J. P. Gleghorn, S. M. Santana, H. Liu, J. P. Smith, V. N. Navarro, S. T. Tagawa, N. H. Bander, D. M. Nanus, and P. A. Giannakakou, PLoS ONE **7**, e35976 (2012).
[4] M. Yu *et al.*, Nature (London) **487**, 510 (2012).
[5] M. Yu *et al.*, Science **339**, 580 (2013).
[6] E. D. Pratt, C. Huang, B. G. Hawkins, J. P. Gleghorn, and B. J. Kirby, Chem. Eng. Sci. **66**, 1508 (2011).
[7] L. R. Huang, E. C. Cox, R. H. Austin, and J. C. Sturm, Science **304**, 987 (2004).
[8] D. Inglis, J. Davis, R. Austin, and J. Sturm, Lab Chip **6**, 655 (2006).
[9] J. Davis, D. Inglis, K. Morton, D. Lawrence, L. Huang, S. Chou, J. Sturm, and R. Austin, Proc. Natl. Acad. Sci. U.S.A. **103**, 14779 (2006).
[10] K. J. Morton, K. Loutherback, D. W. Inglis, O. K. Tsui, J. C. Sturm, S. Y. Chou, and R. H. Austin, Lab Chip **8**, 1448 (2008).
[11] J. V. Green, M. Radisic, and S. K. Murthy, Anal. Chem. **81**, 9178 (2009).
[12] J. P. Gleghorn, E. D. Pratt, D. Denning, H. Liu, N. H. Bander, S. T. Tagawa, D. M. Nanus, P. A. Giannakakou, and B. J. Kirby, Lab Chip **10**, 27 (2010).
[13] S. L. Stott *et al.*, Sci. Transl. Med. **2**, 25ra23 (2010).
[14] S. Nagrath, L. V. Sequist, S. Maheswaran, D. W. Bell, D. Irimia, L. Ulkus, M. Smith, E. L. Kwak, S. Digurmarthy, A. Muzikansky, P. Ryan, U. Balis, R. G. Tompkins, D. A. Haber, and M. Toner, Nature (London) **450**, 1235 (2007).
[15] B. R. Long, M. Heller, J. P. Beech, H. Linke, H. Bruus, and J. O. Tegenfeldt, Phys. Rev. E **78**, 046304 (2008).
[16] J. P. Beech and J. O. Tegenfeldt, Lab Chip **8**, 657 (2008).
[17] M. Heller and H. Bruus, J. Micromech. Microeng. **18**, 075030 (2008).
[18] M. Balvin, E. Sohn, T. Iracki, G. Drazer, and J. Frechette, Phys. Rev. Lett. **103**, 078301 (2009).
[19] J. Frechette and G. Drazer, J. Fluid Mech. **627**, 379 (2009).
[20] K. Loutherback, J. Puchalla, R. H. Austin, and J. C. Sturm, Phys. Rev. Lett. **102**, 045301 (2009).
[21] K. Loutherback, K. S. Chou, J. Newman, J. Puchalla, R. H. Austin, and J. C. Sturm, Microfluid. Nanofluid. **9**, 1143 (2010).
[22] J. P. Smith, A. C. Barbati, S. M. Santana, J. P. Gleghorn, and B. J. Kirby, Electrophoresis **33**, 3133 (2012).
[23] L. Munn and M. Dupin, Ann. Biomed. Eng. **36**, 534 (2008).
[24] D. Leighton and A. Acrivos, J. Fluid Mech. **177**, 109 (1987).
[25] A. Acrivos, G. Batchelor, E. Hinch, D. Koch, and R. Mauri, J. Fluid Mech. **240**, 651 (1992).
[26] A. Acrivos, J. Rheol. **39**, 813 (1995).
[27] Y. Wang, R. Mauri, and A. Acrivos, J. Fluid Mech. **357**, 279 (1998).
[28] J. J. Bishop, A. S. Popel, M. Intaglietta, and P. C. Johnson, Am. J. Physiol. Heart Circ. Physiol. **283**, H1985 (2002).
[29] E. C. Eckstein, D. G. Bailey, and A. H. Shapiro, J. Fluid Mech. **79**, 191 (1977).
[30] X. Grandchamp, G. Coupier, A. Srivastav, C. Minetti, and T. Podgorski, Phys. Rev. Lett. **110**, 108101 (2013).
[31] G. P. Krishnan, S. Beimfohr, and D. T. Leighton, J. Fluid Mech. **321**, 371 (1996).
[32] L. R. Huang, P. Silberzan, J. O. Tegenfeldt, E. C. Cox, J. C. Sturm, R. H. Austin, and H. Craighead, Phys. Rev. Lett. **89**, 178301 (2002).
[33] M. Cabodi, Y. Chen, S. Turner, H. Craighead, and R. H. Austin, Electrophoresis **23**, 3496 (2002).